



Phonon vortex dynamics in graphene ribbon by solving Boltzmann transport equation with *ab initio* scattering rates

Yangyu Guo^a, Zhongwei Zhang^{a,b}, Masahiro Nomura^a, Sebastian Volz^{a,c}, Moran Wang^{d,*}

^aInstitute of Industrial Science, The University of Tokyo, Tokyo 153-8505, Japan

^bCenter for Phononics and Thermal Energy Science, School of Physics Science and Engineering, Tongji University, Shanghai 200092, China

^cLIMMS, CNRS-IIS UMI 2820, The University of Tokyo, Tokyo 153-8505, Japan

^dDepartment of Engineering Mechanics, Tsinghua University, Beijing 100084, China

ARTICLE INFO

Article history:

Received 9 October 2020

Revised 21 December 2020

Accepted 10 January 2021

ABSTRACT

In this work, we study thermal phonon vortex in graphene ribbon by a discrete-ordinate solution of phonon Boltzmann equation under Callaway's dual relaxation model. The phonon scattering rates of normal and resistive processes are acquired from *ab initio* calculation without need of any empirical input parameters. The temperature, size and isotope effects on transition from phonon vortex transport to conventional Fourier's heat conduction in both simple and complex geometries are investigated. The physical mechanism for the evolution of phonon vortex is declared by wide phonon mean free path distribution of resistive processes. A hierarchical vortex series is obtained with primary, secondary and tertiary vortices in a complicated geometry. The present work provides an accurate and efficient multi-scale numerical framework for modeling hydrodynamic phonon transport in high-thermal-conductivity materials and also sheds light on the heat dissipation applications.

© 2021 Elsevier Ltd. All rights reserved.

1. Introduction

With rapid developments of nano-fabrication and manufacturing technologies, the characteristic size of semiconductor electronics drops down to micro- and nano-meter scale nowadays [1,2]. Heat dissipation at such a small confined space becomes a bottleneck of further developments of micro- and nano-electronics in the future [3,4]. To tackle this challenge of thermal management, there have been extensive studies on heat transport at nanoscale and in nanomaterials in the past decades [5-9]. One of the crucial issues is to seek materials with a high thermal conductivity, among which the two-dimensional (2D) graphene [10,11] is a very promising candidate and has demonstrated good performances in cooling down the chips in lab experiments [12,13]. Recent first-principle (*ab initio*) studies [14,15] have declared that the predominance of non-resistive normal phonon scattering over the Umklapp scattering is the main mechanism for the high thermal conductivity of graphene. Hydrodynamic phonon transport, which usually occurs at an extremely low temperatures (~10K) in 3D materials [6], becomes significant in graphitic materials even at moderate temper-

ature (~100K) [16] due to both high Debye temperature and strong anharmonicity [17].

In recent years there are increasing interests in modeling hydrodynamic phonon transport in graphene ribbon. As a first step, previous works were mainly focused on the temperature profile and thermal conductivity (or thermal resistance) of in-plane [18-20] and cross-plane [21,22] heat transport in relatively simpler rectangular geometries. Besides, most works considered the steady-state hydrodynamic phonon transport whereas the transient transport was studied only in few works [23-25]. As phonon transport in the hydrodynamic regime is very similar to viscous fluid flow [6,26], it is expected that the vortex phenomenon of phonons may also take place in crystals. Yet the phonon vortex has attracted rarer attention, in comparison to the wide investigation and understanding of electron vortex in graphene ribbons [27-29]. There is a demonstration of heat vortex in a rectangular graphene ribbon based on macroscopic phonon hydrodynamic equation in a very recent work [30]. However, it remains to consider more realistic material properties due to the challenge of including frequency-dependent phonon scattering rates (or relaxation times) in developing the phonon hydrodynamic equation. In addition, a more thorough analysis and a consideration of more complex geometries pertinent to actual applications is pending, which is one of the main aims of the present work.

* Corresponding author.

E-mail addresses: yyguo@iis.u-tokyo.ac.jp, yangyuhguo@gmail.com (Y. Guo), mrwang@tsinghua.edu.cn, moralwang@gmail.com (M. Wang).

The theoretical modeling of hydrodynamic phonon transport is usually based on the phonon Boltzmann equation. Regarding the treatment of the scattering term in the Boltzmann transport equation, there are mainly two strategies: (i) the full integral scattering term, (ii) relaxation time approximations. In the first strategy, the homogenous solution is obtained by iterative or variational approaches with an empirical phonon-boundary scattering term [14,15,31-33]. A Monte Carlo (MC) scheme has been developed to directly solve the phonon Boltzmann equation under full scattering term [34], yet it is very computationally expensive [19,20]. The relaxation time approximations represent more feasible models for convenient engineering applications. The single mode relaxation time (SMRT) approximation has been shown to much underestimate the thermal conductivity of graphene due to the strong normal scattering [14,31-33]. In comparison, the Callaway's dual relaxation model [35], which treats the normal scattering and Umklapp scattering separately, is a far better approximation to the full scattering term [14,36]. Although the Callaway's model has already been widely used in modeling or analyzing hydrodynamic phonon transport [19,21-23,37-39], the direct numerical solution of phonon Boltzmann equation under Callaway's scattering term has been advanced only recently [18,21,24,25]. Several numerical schemes have been developed including the deterministic discrete-ordinate method (DOM) [18] and discrete unified gas kinetic scheme (DUGKS) [24], as well as the stochastic MC methods [21,25]. However, the empirical scattering rates [18,24] or constant scattering rates [21,25] of normal and Umklapp processes were adopted in these direct numerical solutions. Therefore, another aim of this work is to develop a numerical framework by the input of *ab initio* normal and Umklapp scattering rates into the DOM scheme developed in our previous work [18]. The DOM solution of *ab initio* Callaway's dual relaxation model will be a more accurate description of hydrodynamic phonon transport in graphene. With this numerical framework, we will investigate the phonon vortex dynamics in graphene ribbon in a systematic way.

The remainder of this article will be organized as follows: the mathematical and numerical models will be introduced in Section 2, including the phonon Boltzmann equation under Callaway's model and the DOM scheme with *ab initio* scattering rates. The numerical framework will be validated in Section 3 by two classical cases of heat transport in the graphene ribbon. In Section 4, the phonon vortex dynamics in the graphene ribbon with both rectangular and more complicated geometries will be explored. The concluding remarks are finally made in Section 5.

2. Mathematical and numerical models

In this section, the phonon Boltzmann equation under Callaway's dual relaxation model is presented in Section 2.1. The discrete-ordinate method is introduced to the direct numerical solution of the phonon Boltzmann equation in Section 2.2. Finally, in Section 2.3, the extraction of phonon resistive and normal scattering rates in the Boltzmann equation from *ab initio* calculation is elucidated.

2.1. Phonon Boltzmann equation under Callaway's model

The phonon Boltzmann equation under Callaway's dual relaxation model is adopted [18,35]:

$$\frac{\partial f_{\omega}}{\partial t} + \mathbf{v}_{\mathbf{g}} \cdot \nabla f_{\omega} = \frac{f_{\mathbf{R}}^{\text{eq}}(T_{\text{loc,R}}) - f_{\omega}}{\tau_{\mathbf{R}}(\omega, \mathbf{p}, T)} + \frac{f_{\mathbf{N}}^{\text{eq}}(T_{\text{loc,N}}, \mathbf{u}) - f_{\omega}}{\tau_{\mathbf{N}}(\omega, \mathbf{p}, T)}, \quad (1)$$

where the non-equilibrium distribution function of phonon mode (ω, \mathbf{p}) is abbreviated as $f_{\omega} \equiv f(t, \mathbf{r}, \omega, \mathbf{p}, \mathbf{\Omega})$, and $\mathbf{v}_{\mathbf{g}}$ is the phonon group velocity, $\mathbf{\Omega} = \mathbf{v}_{\mathbf{g}}/v_{\mathbf{g}}$ being the unit vector along the phonon

propagation direction. The relaxation times of resistive and normal phonon scattering processes are denoted by $\tau_{\mathbf{R}}(\omega, \mathbf{p}, T)$ and $\tau_{\mathbf{N}}(\omega, \mathbf{p}, T)$, with their local equilibrium distribution functions respectively defined as:

$$f_{\mathbf{R}}^{\text{eq}}(T_{\text{loc,R}}) = \frac{1}{\exp(\hbar\omega/k_{\text{B}}T_{\text{loc,R}}) - 1}, \quad (2)$$

$$f_{\mathbf{N}}^{\text{eq}}(T_{\text{loc,N}}, \mathbf{u}) = \frac{1}{\exp[(\hbar\omega - \hbar\mathbf{k} \cdot \mathbf{u})/k_{\text{B}}T_{\text{loc,N}}] - 1}, \quad (3)$$

with $T_{\text{loc,R}}, T_{\text{loc,N}}$ the local pseudo-temperatures and \mathbf{u} the local phonon drift velocity, which are determined by the energy and momentum conservation conditions of scattering processes as to be introduced later. Note that the two pseudo-temperatures are introduced as mediate mathematical quantities to ensure the energy conservation of relaxation-type scattering term [40]. The unique local temperature T defined later from the local energy density represents the physical temperature of the phonon system. \mathbf{k} is the phonon wave vector, whereas k_{B} and \hbar denotes separately the Boltzmann constant and reduced Planck constant. The resistive processes considered in this work include three-phonon Umklapp scattering and isotope phonon scattering.

Under the assumption of a small temperature difference throughout the system, the linearized deviational intensity form of Equation (1) is obtained:

$$\frac{\partial \phi_{\omega,\mathbf{p}}}{\partial t} + \mathbf{v}_{\mathbf{g}} \cdot \nabla \phi_{\omega,\mathbf{p}} = \frac{\phi_{\mathbf{R}}^{\text{eq}}(T_{\text{loc,R}}) - \phi_{\omega,\mathbf{p}}}{\tau_{\mathbf{R}}(\omega, \mathbf{p}, T_0)} + \frac{\phi_{\mathbf{N}}^{\text{eq}}(T_{\text{loc,N}}, \mathbf{u}) - \phi_{\omega,\mathbf{p}}}{\tau_{\mathbf{N}}(\omega, \mathbf{p}, T_0)}, \quad (4)$$

where the deviational phonon intensity is introduced as: $\phi_{\omega,\mathbf{p}} = I_{\omega,\mathbf{p}} - I_{\mathbf{R}}^{\text{eq}}(T_0)$, with the phonon intensity [41,42] defined for 2D case as: $I_{\omega,\mathbf{p}} = v_{\mathbf{g}} \hbar \omega f_{\omega} \frac{D(\omega,\mathbf{p})}{2\pi}$, and $I_{\mathbf{R}}^{\text{eq}}(T_0) = v_{\mathbf{g}} \hbar \omega f_{\mathbf{R}}^{\text{eq}}(T_0) \frac{D(\omega,\mathbf{p})}{2\pi}$. $D(\omega, \mathbf{p})$ is the density of states and T_0 is the average system temperature. The linearized expressions of local pseudo-equilibrium deviational phonon intensities for the resistive and normal processes are derived from Equations (2) and (3) respectively [18]:

$$\phi_{\mathbf{R}}^{\text{eq}}(T_{\text{loc,R}}) = v_{\mathbf{g}} \frac{C_{\omega,\mathbf{p}}}{2\pi} (T_{\text{loc,R}} - T_0), \quad (5)$$

$$\phi_{\mathbf{N}}^{\text{eq}}(T_{\text{loc,N}}, \mathbf{u}) = v_{\mathbf{g}} \frac{C_{\omega,\mathbf{p}}}{2\pi} (T_{\text{loc,N}} - T_0) + v_{\mathbf{g}} \frac{C_{\omega,\mathbf{p}}}{2\pi} T_{\text{loc,N}} \frac{\mathbf{k} \cdot \mathbf{u}}{\omega}, \quad (6)$$

where the spectral heat capacity per unit area of 2D materials is: $C_{\omega,\mathbf{p}} = \hbar \omega \frac{\partial f_{\omega}^{\text{eq}}}{\partial T} D(\omega, \mathbf{p})$. The local pseudo-temperatures are determined by the energy conservation condition of resistive and normal processes:

$$T_{\text{loc,R}} - T_0 = \frac{1}{C_{\tau_{\mathbf{R}}}} \sum_{\mathbf{p}} \int \int_0^{2\pi} \frac{\phi_{\omega,\mathbf{p}}}{\Lambda_{\mathbf{R}}(\omega, \mathbf{p}, T_0)} d\theta d\omega, \quad (7)$$

$$T_{\text{loc,N}} - T_0 = \frac{1}{C_{\tau_{\mathbf{N}}}} \sum_{\mathbf{p}} \int \int_0^{2\pi} \frac{\phi_{\omega,\mathbf{p}}}{\Lambda_{\mathbf{N}}(\omega, \mathbf{p}, T_0)} d\theta d\omega, \quad (8)$$

where $C_{\tau_{\mathbf{R}}} = \sum_{\mathbf{p}} \int \frac{C_{\omega,\mathbf{p}}}{\tau_{\mathbf{R}}(\omega,\mathbf{p},T_0)} d\omega$ and $C_{\tau_{\mathbf{N}}} = \sum_{\mathbf{p}} \int \frac{C_{\omega,\mathbf{p}}}{\tau_{\mathbf{N}}(\omega,\mathbf{p},T_0)} d\omega$ are introduced for short notation, and $\theta \in [0, 2\pi]$ is the angular variable of phonons in the 2D case. The phonon mean free path (MFP) of resistive and normal processes are respectively $\Lambda_{\mathbf{R}}(\omega, \mathbf{p}, T_0) = v_{\mathbf{g}}(\omega, \mathbf{p}) \tau_{\mathbf{R}}(\omega, \mathbf{p}, T_0)$ and $\Lambda_{\mathbf{N}}(\omega, \mathbf{p}, T_0) = v_{\mathbf{g}}(\omega, \mathbf{p}) \tau_{\mathbf{N}}(\omega, \mathbf{p}, T_0)$. The local phonon drift velocity is determined by the quasi-momentum conservation condition of normal process:

$$\mathbf{u} = \frac{2}{T_{\text{loc,N}} C_{\tau_{\mathbf{N}}}} \sum_{\mathbf{p}} \int \int_0^{2\pi} \frac{\mathbf{k}}{\omega} \frac{\phi_{\omega,\mathbf{p}}}{\Lambda_{\mathbf{N}}(\omega, \mathbf{p}, T_0)} d\theta d\omega, \quad (9)$$

where $C_{\tau_{\mathbf{N}}}^1 = \sum_{\mathbf{p}} \int \frac{k^2}{\omega^2} \frac{C_{\omega,\mathbf{p}}}{\tau_{\mathbf{N}}(\omega,\mathbf{p},T_0)} d\omega$ is introduced for short notation.

The isotropic phonon properties are implicitly assumed in the Boltzmann transport model Eqs. (4)-(9). After the deviational phonon intensity in Equation (4) is resolved, the macroscopic field variables (temperature T and heat flux \mathbf{q}) are computed through a statistical integration:

$$e^d(t, \mathbf{r}) = \frac{1}{h_0} \sum_p \int \int_0^{2\pi} \frac{\phi_{\omega,p}}{v_g} d\theta d\omega = C_V [T(t, \mathbf{r}) - T_0], \quad (10)$$

$$\mathbf{q}(t, \mathbf{r}) = \frac{1}{h_0} \sum_p \int \int_0^{2\pi} \phi_{\omega,p} \mathbf{\Omega} d\theta d\omega, \quad (11)$$

where e^d denotes the local deviational energy density, with h_0 the thickness of 2D materials, and the specific heat per unit volume for 2D materials defined as: $C_V = \frac{1}{h_0} \sum_p \int C_{\omega,p} d\omega$.

2.2. Discrete-ordinate method

In this work, we consider 2D steady-state phonon transport, for which Equation (4) is reduced to:

$$\mu \frac{\partial \phi_{\omega,p}}{\partial x} + \eta \frac{\partial \phi_{\omega,p}}{\partial y} = \frac{\phi_R^{\text{eq}}(T_{\text{loc,R}}) - \phi_{\omega,p}}{\Lambda_R(\omega, p, T_0)} + \frac{\phi_N^{\text{eq}}(T_{\text{loc,N}}, u_x, u_y) - \phi_{\omega,p}}{\Lambda_N(\omega, p, T_0)}, \quad (12)$$

where the directional cosine and sine are defined as: $\mu = \cos \theta$, $\eta = \sin \theta$. A discrete-ordinate method has been developed for a direct numerical solution of Equation (12) in our previous work [18]. The main idea will be explained here without a repetition of all the technical details. The spectral and angular spaces are discretized based on the Gauss-Legendre (G-L) quadrature, with the number of abscissae N_p (for phonon branch p) and N_θ respectively. The discrete form of Equation (12) in spectral and angular spaces thus becomes:

$$\mu_k \frac{\partial (\phi_p)_n^k}{\partial x} + \eta_k \frac{\partial (\phi_p)_n^k}{\partial y} = \frac{(\phi_{pR}^{\text{eq}})_n - (\phi_p)_n^k}{(\Lambda_{pR})_n} + \frac{(\phi_{pN}^{\text{eq}})_n - (\phi_p)_n^k}{(\Lambda_{pN})_n}, \quad (13)$$

where $k = 1, 2, \dots, N_\theta$ and $n = 1, 2, \dots, N_p$ denote the index of discrete angular and spectral nodes. The step scheme [43] is adopted for the spatial discretization to ensure both numerical accuracy and stability. For the first quadrant of angular space with $\mu > 0$, $\eta > 0$, the forward difference scheme is applied to both x -direction and y -direction spatial derivatives in Equation (13):

$$\begin{aligned} \mu_k \frac{(\phi_p)_{n,i,j}^k - (\phi_p)_{n,i-1,j}^k}{\Delta x} + \eta_k \frac{(\phi_p)_{n,i,j}^k - (\phi_p)_{n,i,j-1}^k}{\Delta y} \\ = \frac{(\phi_{pR}^{\text{eq}})_{n,i,j} - (\phi_p)_{n,i,j}^k}{(\Lambda_{pR})_n} + \frac{(\phi_{pN}^{\text{eq}})_{n,i,j} - (\phi_p)_{n,i,j}^k}{(\Lambda_{pN})_n}, \end{aligned} \quad (14)$$

where Δx and Δy are the spatial steps. For the other three quadrants of angular space, the spatial discretization scheme is similar, with the details given in Ref. [18]. The following evolution equation of the discrete deviational phonon intensity for $\mu > 0$, $\eta > 0$ is derived from Equation (14) as:

$$\begin{aligned} (\phi_p)_{n,i,j}^k \\ = \frac{(m_p)_n^k (\phi_p)_{n,i-1,j}^k + (n_p)_n^k (\phi_p)_{n,i,j-1}^k + \frac{(\Lambda_{pR})_n}{\Delta x} (\phi_{pR}^{\text{eq}})_{n,i,j} + \frac{(\Lambda_{pN})_n}{\Delta y} (\phi_{pN}^{\text{eq}})_{n,i,j}}{(m_p)_n^k + (n_p)_n^k + 1}, \end{aligned} \quad (15)$$

where $(m_p)_n^k = \frac{\mu_k (\Lambda_{pR})_n}{\Delta x}$, $(n_p)_n^k = \frac{\eta_k (\Lambda_{pN})_n}{\Delta y}$ are introduced for short notation, and the overall phonon mean free path is defined based on the Mathiessen's rule as: $\frac{1}{\Lambda_{pR}} = \frac{1}{\Lambda_{pR}} + \frac{1}{\Lambda_{pN}}$. The subscripts $i = 1, 2, \dots, N_x$ and $j = 1, 2, \dots, N_y$ denotes the index of spatial nodes,

with N_x and N_y the number of spatial grids along x -direction and y -direction respectively.

The DOM numerical solution is implemented through an iteration process. Within each iteration step, the deviational phonon intensity for $\mu > 0$, $\eta > 0$ is updated from the left-bottom boundaries of the system based on Equation (15). The update is done through similar procedures for the other three quadrants of angular space [18]. Then the pseudo-equilibrium deviational phonon intensities for normal and resistive processes are computed based on Eqs. (5)-(9). The iteration process is terminated until the relative difference of pseudo-equilibrium deviational intensities between two successive iteration steps is smaller than 1×10^{-10} . After the convergence of deviational phonon intensity, the macroscopic field variables are calculated based on Equations (10) and (11).

2.3. Ab initio scattering rates

In this work, the phonon properties of mono-layer graphene including the phonon dispersion and scattering rates are computed from *ab initio* (or DFT, density functional theory) calculation, which represents a more accurate description than the empirical expressions in previous work [18,24]. The *ab initio* calculation is implemented in the open-source package QUANTUM ESPRESSO (QE) [44]. The norm-conserving pseudopotential with LDA (local density approximation) exchange-correlation functional is adopted as recommended by a recent benchmark study [45]. A convergence threshold of 10^{-12} is used for the self-consistent field calculation. The lattice constant of graphene is obtained as 2.4403 Å through a unit cell relaxation in QE with a kinetic energy cutoff of 120Ry for the wave function, and a convergence threshold of 10^{-7} a.u. (atomic unit) and 10^{-4} a.u. for the total energy and force respectively. The value of lattice constant agrees well with the result in the literature [45,46] with the same pseudopotential and functional. An accurate lattice constant is crucial for graphene since its tiny change will give rise to a considerable variation of thermal transport properties [46]. A vacuum layer of 20 Å is used in the out-of-plane direction to avoid any spurious interaction between adjacent graphene layers in the supercell calculation. The finite displacement method is adopted to compute the harmonic force constants (FCs) as implemented in the open-source package PHONOPY [47]. A sufficiently large supercell of $10 \times 10 \times 1$ (200 atoms) is used to ensure capturing the long-range two-body interaction in graphene. A kinetic energy cutoff of 120Ry for the wave function and an electronic wave vector grid of $4 \times 4 \times 1$ are adopted in the DFT calculation in QE. The third-order FCs are also computed by the finite displacement method as implemented in the open-source script THIRDDORDER [48]. A supercell of $9 \times 9 \times 1$ (162 atoms) is used, with the six nearest neighbor atomic interaction included. A kinetic energy cutoff 100Ry for wave function is adopted in the Γ -point DFT calculation in QE. After extracting the harmonic and third-order FCs, the phonon thermal properties (phonon dispersion, scattering rates, thermal conductivity, etc.) of graphene are calculated in the open-source package SHENGBTE [48] with a phonon wave vector grid of $100 \times 100 \times 1$ after independence verification. The scattering rates of normal process and Umklapp process are distinguished by the conservation of phonon quasi-momentum or not based on a revised SHENGBTE code.

As the full first Brillouin zone (BZ) is considered in the *ab initio* calculation of phonon properties, some treatment is done to input them into the present isotropic Boltzmann equation solver. Since the anisotropy within the in-plane direction of graphene is very weak, we adopt the *ab initio* phonon properties along the high-symmetry Γ -M direction in the DOM solution. The phonon dispersion along Γ -M direction is shown in Fig. 1. The scattering rates of normal process and Umklapp process at 100K in the

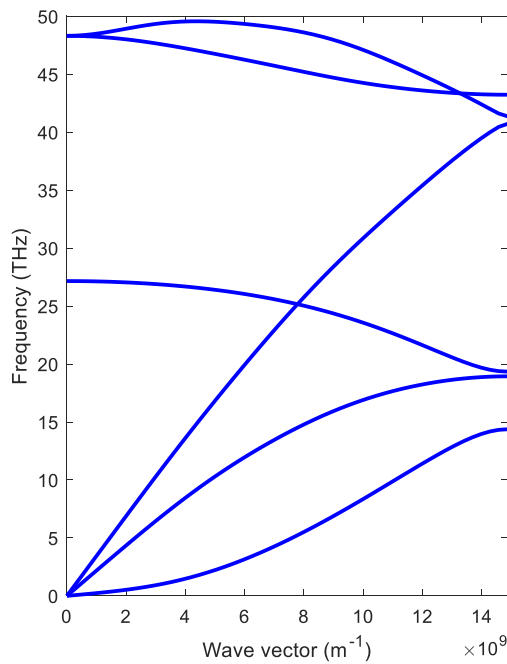


Fig. 1. Phonon dispersion of graphene along Γ -M direction from *ab initio* calculation.

full first BZ and along Γ -M direction are shown in Fig. 2(a) and (b) respectively. The scattering rates along Γ -M direction demonstrate a good representation of those in the full first BZ. In addition, the normal scattering rate is much larger than the Umklapp scattering rate for the low- and moderate-frequency phonons, which indicates very strong hydrodynamic phonon transport at 100K. Furthermore, we omit the optical phonons in the DOM solution due to the following considerations: (i) the contribution of optical phonons to heat transport is very small in the concerned low-temperature hydrodynamic regime; (ii) the present DOM scheme needs to be further adjusted to treat the negative phonon group velocity ($v_g = d\omega/dk < 0$) of optical phonons along the transport direction. As a validation of the present isotropic Callaway's model with *ab initio* phonon properties, we show the bulk thermal conductivities of isotopically pure and natural abundance graphene in Fig. 3(a) and (b) respectively. For the natural abundance case in Fig. 3(b), the good agreement between the present iterative solution of phonon Boltzmann equation under full scattering term and a previous variational solution with FCs computed by QE using the same pseudo-potential and functional [14] demonstrates the reliability of the present *ab initio* calculation. For both cases, the SMRT model much underestimates the bulk thermal conductivity of graphene obtained by the iterative solution, as consistent with the trend in previous works [14,31-33]. In contrast, the result by the Callaway's model in the full first BZ or in the present isotropic assumption shows an overall good agreement with the iterative solution within around 30% relative error. As an intuitive comparison, for isotopically pure graphene at 100K, the isotropic SMRT model gives a thermal conductivity (837.0544 W/m·K) about two orders of magnitude smaller than the iterative solution (2.0020×10^5 W/m·K) whereas the present isotropic Callaway's model gives a value (1.6421×10^5 W/m·K) with only about 20% underestimation.

3. Methodology validation

The discrete-ordinate method for the phonon Boltzmann equation under Callaway's dual relaxation model has been extensively validated in our previous work [18] based on empirical phonon

properties of graphene. In this section, a quantitative validation will be demonstrated for the DOM numerical scheme with *ab initio* scattering rates introduced in Section 2. Two cases are modeled as shown in Fig. 4: heat transport through infinitely wide graphene ribbon in Section 3.1, and heat transport through infinitely long graphene ribbon in Section 3.2.

3.1. Heat transport through infinitely wide graphene ribbon

In this sub-section, heat transport through an infinitely wide graphene ribbon with a length L is modeled as shown in Fig. 4(a). To have a consistent comparison to available results in the literature, natural abundance (1.1% ^{13}C) of carbon is considered. The average system temperature is $T_0 = 300\text{K}$, with the temperatures of left-hand hot source $T_h = 300.5\text{K}$ and right-hand cold source $T_c = 299.5\text{K}$ respectively. The small temperature difference (1K) ensures the validity of the linearized assumption. In the present case, the DOM scheme is reduced to a one-dimensional formulation. The numerical treatment of isothermal boundary conditions can be found in Ref. [18]. A spatial grid of $N_x = 100$, a spectral grid of $N_L = N_T = N_Z = 10$ for LA, TA and ZA phonons, and an angular grid of $N_\theta = 32$ are adopted after independence verification. After convergence of the deviational phonon intensity, the heat flux q_x across the graphene ribbon is calculated and then the thermal conductivity is computed by: $\kappa = q_x L / (T_h - T_c)$. The length-dependent thermal conductivity of the graphene ribbon is shown in Fig. 5, where an *ab initio* MC solution of phonon Boltzmann equation under full scattering term [34] and a non-equilibrium molecular dynamics (NEMD) simulation result [49] for the same heat transport process are included for comparison. The present DOM solution with *ab initio* (DFT) scattering rates agrees well with the *ab initio* MC solution. The small difference between the present DOM solution and NEMD result may be caused by the fact that empirical atomic interaction potential is adopted in NEMD. The overall good agreement indicates that the present *ab initio* Callaway's scattering model still captures well the heat transport behaviors in micro- and nano-ribbon of graphene.

3.2. Heat transport through infinitely long graphene ribbon

In this sub-section, heat transport through an infinitely long graphene ribbon with a width W and natural abundance at 300K is modeled as shown in Fig. 4(b). A constant uniform temperature gradient of $-dT/dx = -10^8$ K/m is exerted along the transport direction through a periodic heat flux boundary condition. A fully diffuse scheme is implemented for the lateral adiabatic boundary condition. The details of boundary treatment can be found in Ref. [18]. After independence verification, a spatial grid of $N_x = 2$ and $N_y = 100$, a spectral grid of $N_L = N_T = N_Z = 10$ for LA, TA and ZA phonons, and an angular grid of $N_\theta = 96$ are adopted. After the convergence of deviational phonon intensity, the cross-sectional heat flux distribution $q_x(y)$ is calculated and then the thermal conductivity is computed by: $\kappa = \frac{1}{W} \int_0^W q_x(y) dy / (dT/dx)$. The width-dependent thermal conductivity of the graphene ribbon is shown in Fig. 6, where an overall good agreement is obtained between the present DOM solution with *ab initio* (DFT) scattering rates and an *ab initio* MC solution of phonon Boltzmann equation under full scattering term [34]. The minor difference may be caused by the different treatments of phonon scattering term, as well as possible difference between the DFT phonon properties calculated by different groups.

4. Results and discussion

In this section, the DOM numerical framework with *ab initio* scattering rates in Section 2 will be applied to explore the phonon

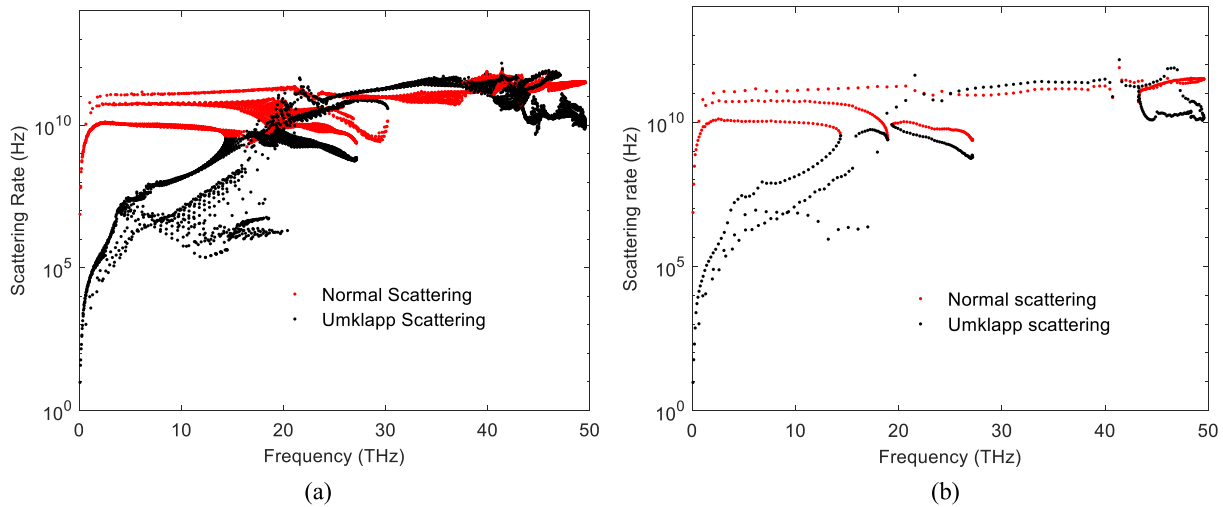


Fig. 2. Ab initio scattering rates of three-phonon normal and Umklapp processes in graphene at 100K: (a) in the full first Brillouin zone, (b) along Γ -M direction. The red points represent the normal scattering whereas the black points represent the Umklapp scattering.

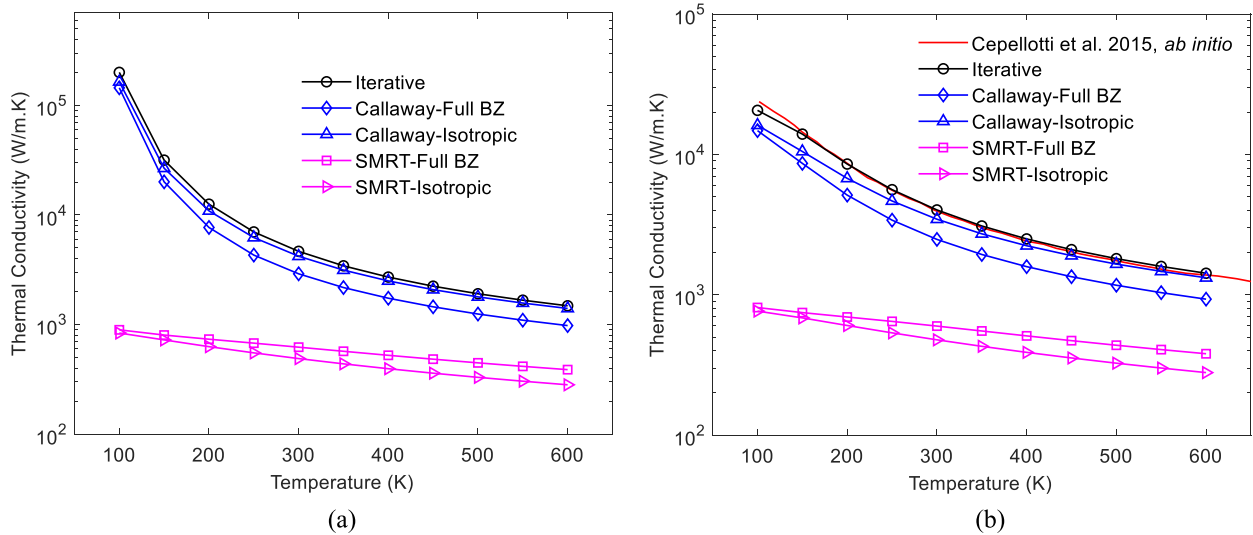


Fig. 3. Temperature-dependent thermal conductivity of bulk graphene: (a) isotopically pure (0% ^{13}C) case, (b) natural abundance (1.1% ^{13}C) case. The circle-line represents the iterative solution of phonon Boltzmann equation under full scattering term, the blue diamond-line and upper-triangle-line represent the result of Callaway's dual relaxation scattering model in the full Brillouin zone (BZ) and in the present isotropic assumption, the magenta square-line and right-triangle-line represent the result of single-mode-relaxation-time (SMRT) scattering model in the full BZ and in the present isotropic assumption. The solid red line represents the result by variational solution of phonon Boltzmann equation under ab initio full scattering term from Ref. [14].

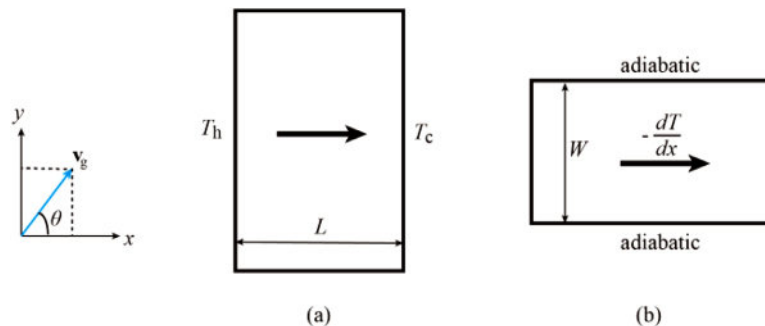


Fig. 4. Schematic of heat transport through graphene ribbon: (a) infinitely wide graphene ribbon with a length L ; (b) infinitely long graphene ribbon with a width W .

vortex dynamics in the graphene ribbon. Two cases will be investigated including a rectangular graphene ribbon in Section 4.1 and a more complicated T-type graphene ribbon in Section 4.2. The graphene ribbons in both cases are perfect as any internal geometrical defects (for instance, grain boundaries, lattice dislocations and pores inside the ribbon) will induce resistive phonon-defect scattering and appreciably destroy the phonon vortex hydrodynamics.

The first case is similar to the physical model in the very recent paper [30], yet we will present a more thorough study on the temperature effect, size effect as well as isotope effect on the dynamics of phonon vortex. The underlying mechanism of the transition from hydrodynamic to diffusive heat transport will be elucidated

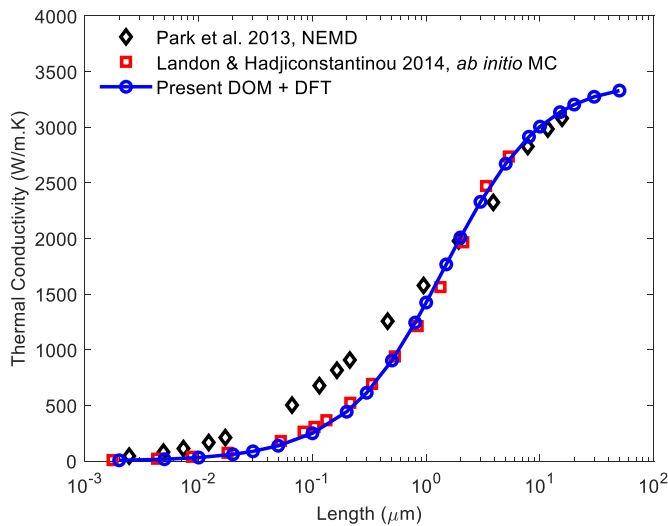


Fig. 5. Length-dependent thermal conductivity of infinitely wide graphene ribbon with natural abundance (1.1% ¹³C) at 300K: the black diamonds represent the result by non-equilibrium molecular dynamics (NEMD) [49], the red squares represent the result by ab initio Monte Carlo (MC) solution of phonon Boltzmann equation under full scattering term [34], the blue circle-line represents the present DOM (discrete-ordinate method) solution of phonon Boltzmann equation under Callaway's dual relaxation model with ab initio (DFT) phonon properties.

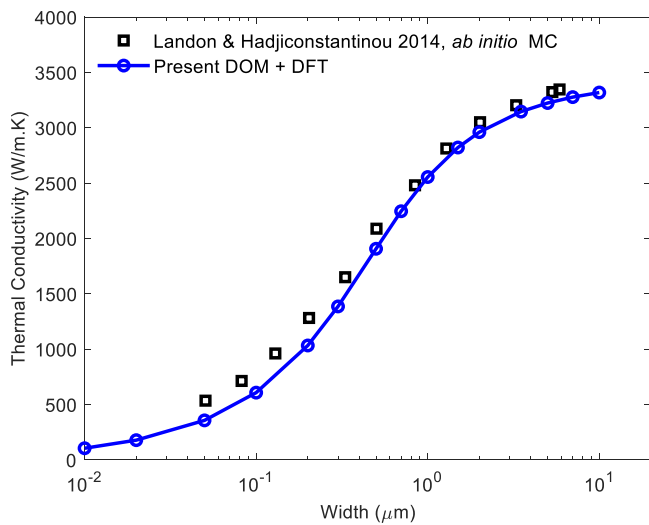


Fig. 6. Width-dependent thermal conductivity of infinitely long graphene ribbon with natural abundance (1.1% ¹³C) at 300K: the black squares represent the result by the ab initio Monte Carlo (MC) solution of phonon Boltzmann equation under full scattering term [34], the blue circle-line represent the result by the present DOM (discrete-ordinate method) solution of phonon Boltzmann equation under Callaway's dual relaxation model with ab initio (DFT) phonon properties.

via the MFP analysis of normal and resistive phonon scattering processes. The second case is a counterpart of the classical lid-driven cavity flow [50] in fluid dynamics. The evolution of phonon vortex configuration with the cavity height-width ratio will be discussed.

4.1. Phonon vortex in rectangular graphene ribbon

In this sub-section, phonon heat transport in a rectangular graphene ribbon with $L = 3W$ is simulated, as shown in Fig. 7. The length of the heat source at the upper edge and the cold source at the lower edge are $L_h = L_c = 1/20L$. A small temperature difference of $T_h - T_c = 1K$ around an average temperature T_0 is exerted on the graphene ribbon. The influence of average temperature T_0 and

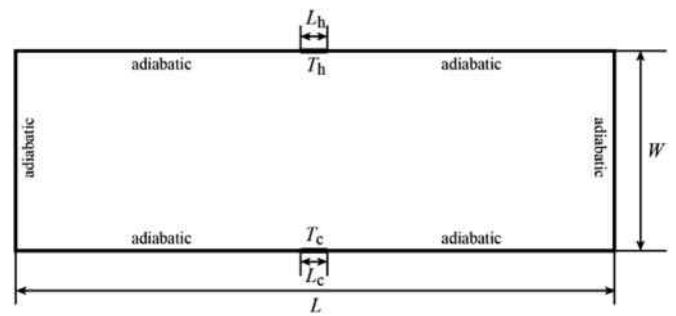


Fig. 7. Schematic of the physical model of phonon vortex in rectangular graphene ribbon.

length L on phonon transport in isotopically pure graphene ribbon is studied in Section 4.1.1, and the influence of isotope phonon scattering will be discussed in Section 4.1.2 by also modeling the graphene ribbon with natural abundance. After independence verification, a spatial grid of $N_x = 240$ and $N_y = 80$, a spectral grid of $NL = NT = 10$ for LA, TA and ZA phonons, and an angular grid of $N_\theta = 48$ are adopted in the DOM numerical solution.

4.1.1. Temperature and size effect

The temperature contour and heat flux streamline in the rectangular graphene ribbon with a fixed length $L = 15\mu m$ at three different average system temperatures $T_0 = 100K, 150K$ and $300K$ are shown in Fig. 8. Two large side phonon vortexes occupying approximately 1/3 of the length respectively are obtained at $T_0 = 100K$ in Fig. 8(a). The vortex has a similar physical picture to the fluid vortex, and can be understood to be generated by the 'viscous force' (quasi-momentum transfer) from the middle mainstream phonons to the side phonons in the confined corner. As the average system temperature increases to $150K$, the size of the vortex is reduced a lot as shown in Fig. 8(b), where two small vortex pairs are also appearing at two sides. At room temperature ($T_0 = 300K$), the phonon heat transport features the typical diffusive behavior predicted by the classical Fourier's law as shown in Fig. 8(c). A clear transition from hydrodynamic to diffusive heat transport is demonstrated from $100K$ to $300K$. In addition, in the hydrodynamic regime, a low-temperature region emerges near the hot source, and a high-temperature region near the cold source. In other words, heat transports from a low temperature place to a high temperature one due to the formation of a vortex. As a result, we obtain a negative non-local temperature response between the upper edge and the lower edge of the graphene ribbon. The size of the anomalous low/high-temperature regions decreases with temperature from $100K$ in Fig. 8(a) to $150K$ in Fig. 8(b). Thus the negative non-local temperature response weakens with increasing temperature and finally becomes reverse, as shown in Fig. 9.

The heat transport from low to high temperatures apparently violates the second law of thermodynamics. To understand this, firstly we revisit the entropy generation expression in diffusive heat conduction [51]: $\sigma^s = \mathbf{q} \cdot \nabla \frac{1}{T}$. The linear Fourier's law of heat conduction $\mathbf{q} = -\kappa \nabla T$ satisfies the second law as it yields $\sigma^s = \mathbf{q}^2 / \kappa T^2 \geq 0$. The Fourier's law indicates the direction of heat flux is opposite to that of temperature gradient, i.e. the heat flux always goes from high to low temperatures. However, in the phonon hydrodynamic regime, the transport mechanism and heat conduction law are different from those in the conventional diffusive regime. One of the well-known heat conduction equations in hydrodynamic regime is the G-K (Guyer-Krumhansl) equation [52]:

$$\tau_R \frac{\partial \mathbf{q}}{\partial t} + \mathbf{q} = -\kappa \nabla T + \frac{1}{5} v_g^2 \tau_N \tau_R [\nabla^2 \mathbf{q} + 2 \nabla (\nabla \cdot \mathbf{q})]. \quad (16)$$

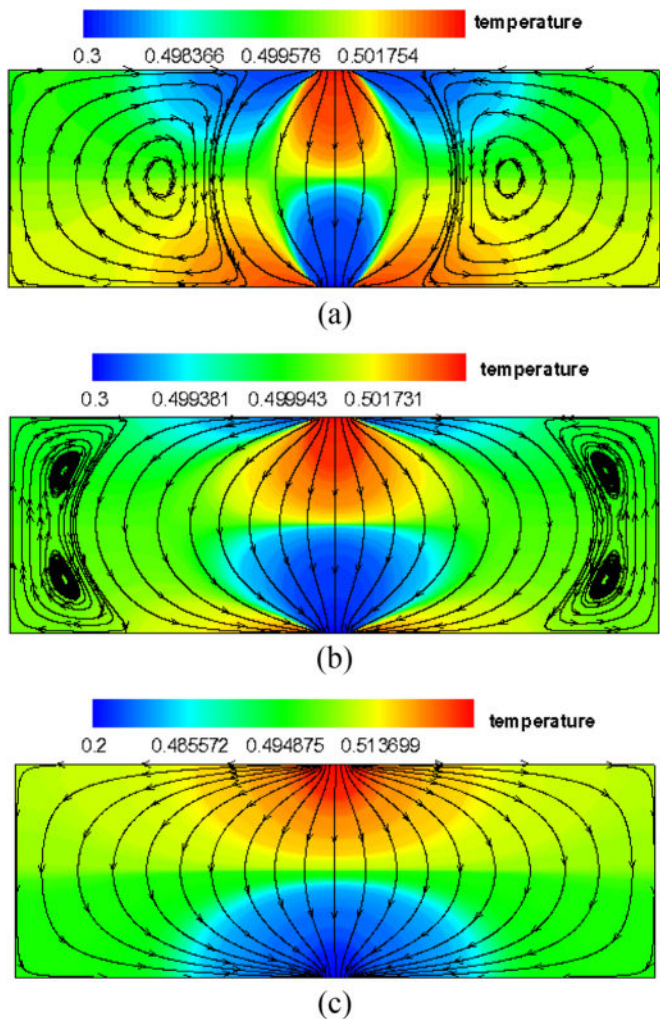


Fig. 8. Phonon vortex dynamics in a rectangular graphene ribbon with $L=3W=15\mu\text{m}$ at different average temperatures: (a) $T_0=100\text{K}$, (b) $T_0=150\text{K}$, (c) $T_0=300\text{K}$. The color contour denotes the distribution of the dimensionless temperature defined as: $\theta=(T-T_c)/(T_h-T_c)$, whereas the streamline denotes the heat flux vector.

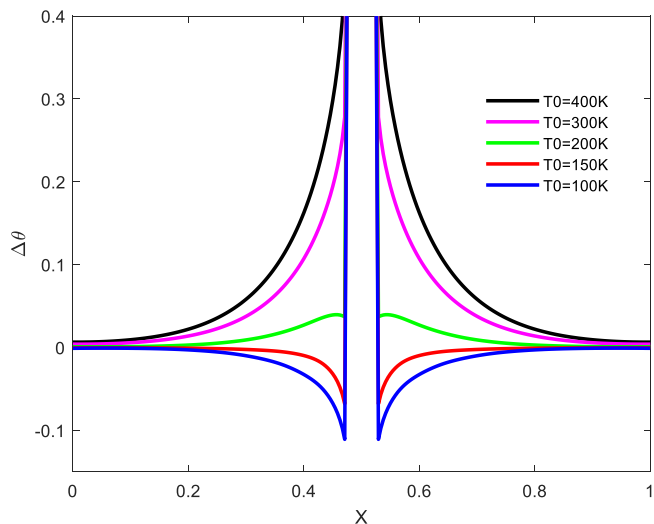


Fig. 9. Non-local temperature response between the upper and lower edge of the rectangular graphene ribbon with $L=3W=15\mu\text{m}$ at different average temperatures. Here $\Delta\theta$ is the difference of dimensionless temperature between the upper edge ($y=W$) and the lower edge ($y=0$).

In the steady-state limit considered in this work, Equation (16) is reduced to:

$$\mathbf{q} = -\kappa \nabla T + \frac{1}{5} v_g^2 \tau_N \tau_R \nabla^2 \mathbf{q}, \quad (17)$$

where the term $\nabla \cdot \mathbf{q}$ vanishes with the help of energy balance equation. As the second non-local term of heat flux on the right-hand side of Equation (17) is significant in the hydrodynamic regime, the heat flux direction is no longer exactly opposite to that of temperature gradient. Thus in principle heat flux can go from low to high temperatures under certain situation, as shown in the present phonon vortex phenomenon. The thermodynamic compatibility of G-K equation has been well verified in the framework of extended irreversible thermodynamics (EIT) [53]. In the EIT framework, the heat flux (\mathbf{q}) and the higher-order flux of heat flux (\mathbf{Q}) will enter the state space in addition to the usual internal energy. The heat flux and its flux play similar roles as the momentum and pressure tensor in non-equilibrium thermodynamics for fluid flow [51,54]. The entropy generation expression in phonon hydrodynamic regime holds a similar form to that in fluid dynamics [6,53]:

$$\sigma^s = \frac{\mathbf{q}^2}{\kappa T^2} + \mu_2 \mathbf{Q}_o : \mathbf{Q}_o + \mu_0 Q^2 \geq 0, \quad (18)$$

where Q and \mathbf{Q}_o are the trace and deviatoric part of \mathbf{Q} (as the counterparts of pressure and stress tensor in fluid dynamics), and the positive-definite coefficients μ_2 and μ_0 are available in Ref. [6,53]. The first term and the last two terms on the right-hand side of Equation (18) represent respectively the contribution to irreversibility from diffusive and hydrodynamic heat conduction. In a word, the negative non-local temperature response is actually still consistent with the second law of thermodynamics.

We also demonstrate the phonon vortex dynamics in rectangular graphene ribbon with different lengths at a fixed average system temperature $T_0 = 100\text{K}$ in Fig. 10. The size of the phonon vortex generally decreases with increasing length of the graphene ribbon in the present range, and the vortex disappears at a length of $120\mu\text{m}$. Thus the magnitude of negative non-local temperature response will also decrease with increasing ribbon size, as shown in Fig. 11. At a very large length of $120\mu\text{m}$, there is still finite negative non-local response within a very small region near the heat source although there is no longer phonon vortex inside the graphene ribbon. This indicates the phonon heat transport is not fully diffusive and some hydrodynamic behavior still remains at such low temperature, which is different from the transition in Fig. 9.

The temperature and size effect on the phonon vortex dynamics in the rectangular graphene ribbon will be interpreted from a phonon MFP analysis. For a specific phonon mode (ω, p), hydrodynamic transport takes place only within a window condition [6,14,52]: $\Lambda_N(\omega, p) \ll L \ll \Lambda_R(\omega, p)$. In Fig. 12, the frequency-dependent MFP of phonon normal and resistive scattering processes throughout the full BZ in isotopically pure graphene at 100K and 300K are displayed. Note that the Umklapp scattering is the only intrinsic resistive phonon scattering here. The MFP distribution of normal process is comparatively uniform to that of resistive process which spreads several orders of magnitude. The MFPs of both normal and resistive processes decrease with increasing temperature because of stronger phonon scattering. Furthermore, the MFP of the resistive process decreases more rapidly than that of the normal process from 100K to 300K, such that the hydrodynamic window becomes narrower. For a graphene ribbon with a length $L=15\mu\text{m}$, phonons with $\omega < \sim 14\text{THz}$ at 100K well lie within the hydrodynamic window. In contrast, at 300K, only a very small portion of phonons at $\omega < \sim 4\text{THz}$ satisfies the window condition. This provides a basic explanation of the transition from hydrodynamic to diffusive heat transport with increasing tempera-

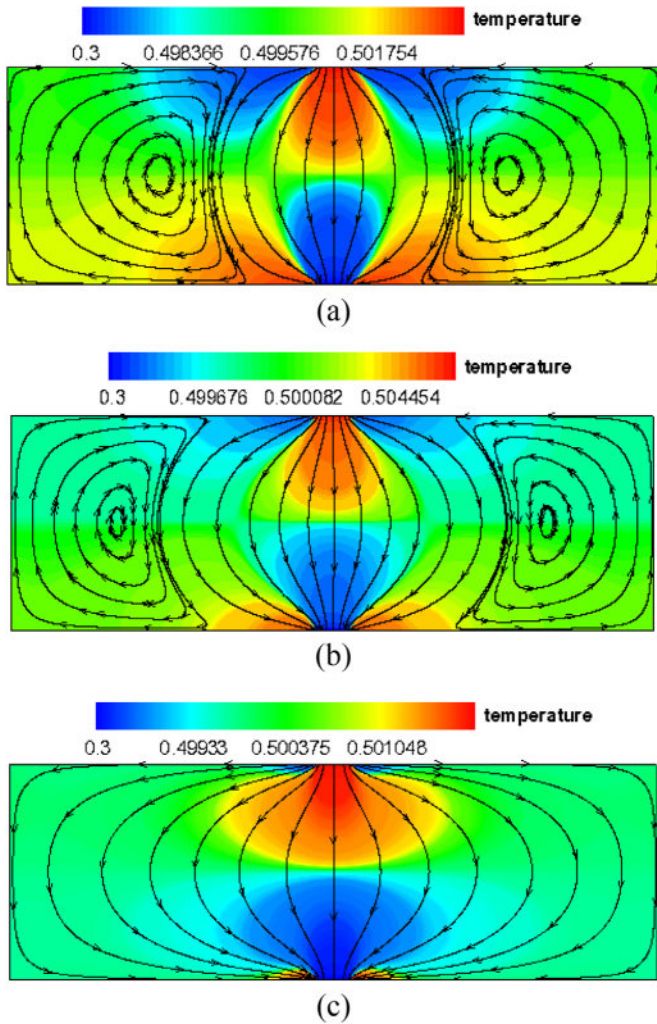


Fig. 10. Phonon vortex dynamics in rectangular graphene ribbon with different sizes at average temperature 100K: (a) $L=3W=15\mu\text{m}$, (b) $L=3W=60\mu\text{m}$, (c) $L=3W=120\mu\text{m}$. The color contour denotes the distribution of the dimensionless temperature defined as: $\theta=(T-T_c)/(T_h-T_c)$, whereas the streamline denotes the heat flux vector.

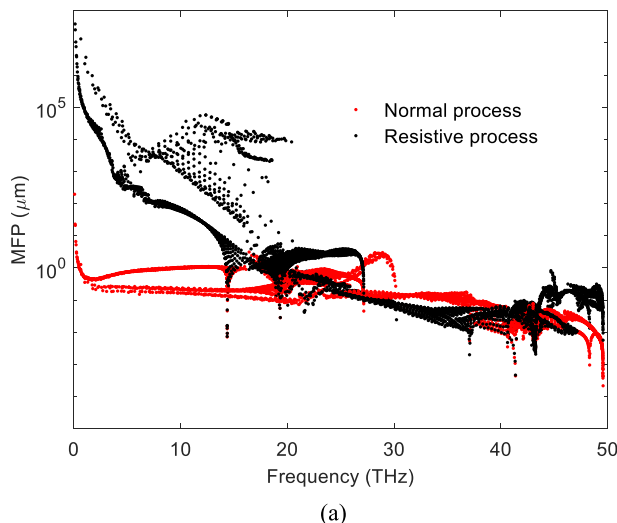


Fig. 12. Frequency-dependent phonon mean free path (MFP) of normal and resistive processes in isotopically pure (0% ^{13}C) graphene at different temperatures: (a) 100K, (b) 300K. The red points denote the normal process whereas the black points denote the resistive process.

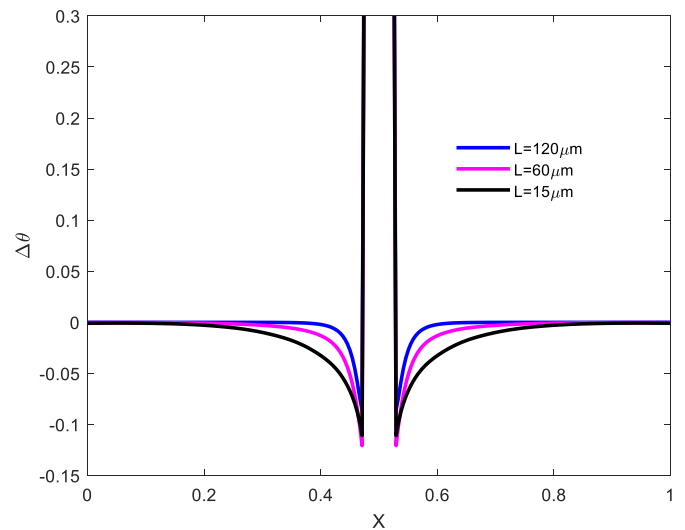


Fig. 11. Non-local temperature response between the upper and lower edge of the rectangular graphene ribbon with different sizes ($L=3W$) at average temperature 100K. Here $\Delta\theta$ is the difference of dimensionless temperature between the upper edge ($y=W$) and the lower edge ($y=0$).

ture shown in Fig. 8 and Fig. 9. To have a deeper understanding, we also calculate an average MFP of normal and resistive processes as:

$$\langle \Lambda \rangle = \frac{\frac{1}{\hbar_0} \sum_p \int C_{q,p} \Lambda_{q,p} \frac{dq}{(2\pi)^2}}{C_V}, \quad (19)$$

with the modal heat capacity $C_{q,p} = \hbar\omega \partial f_R^{eq} / \partial T$ as the weight for average. The results of temperature-dependent average MFP and the weight are shown in Fig. 13. The good consistency between the full BZ result and the isotropic result in Fig. 13(a) demonstrates again the validity of the isotropic assumption in this work. As inferred from Fig. 13(b), the phonons with $\omega < \sim 14\text{THz}$ dominate the contribution to average MFP and heat transport at 100K. In comparison, at 300K, there are still appreciable phonons at $\omega > \sim 4\text{THz}$ that contribute to the average MFP and heat transport. Although the overall average MFP of the resistive process ($\sim 500\mu\text{m}$) is still much larger than the ribbon length ($15\mu\text{m}$), these phonons ($\omega > \sim 4\text{THz}$) with resistive scattering MFP comparable to the rib-

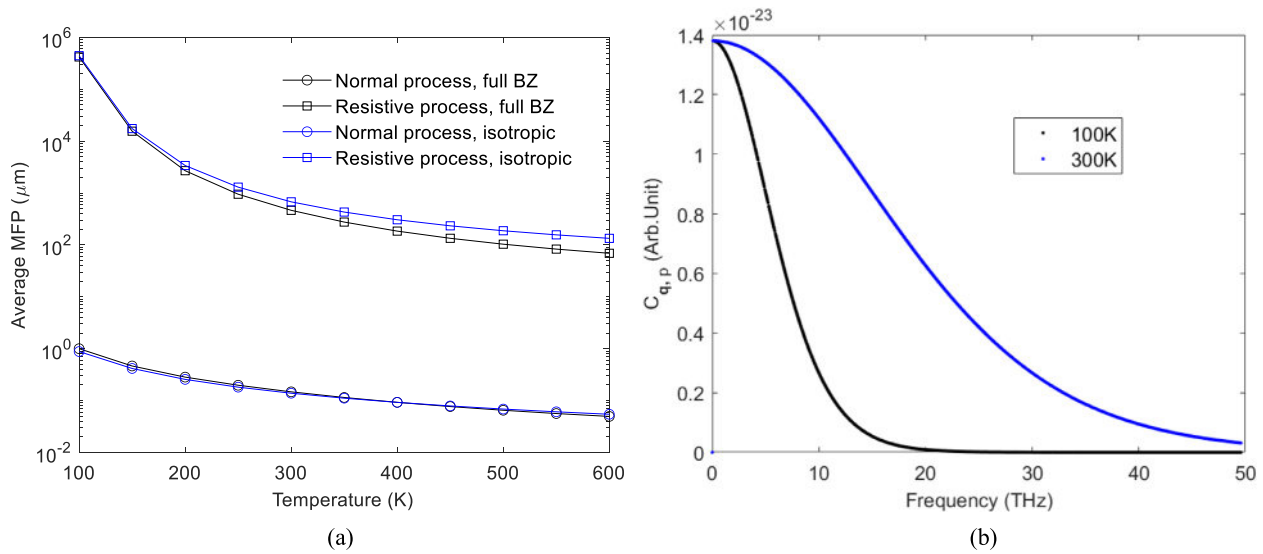


Fig. 13. Temperature-dependent average phonon mean free path (MFP) of normal and resistive processes in isotopically pure (0% ^{13}C) graphene: (a) average MFP, (b) the modal heat capacity as the weight for average.

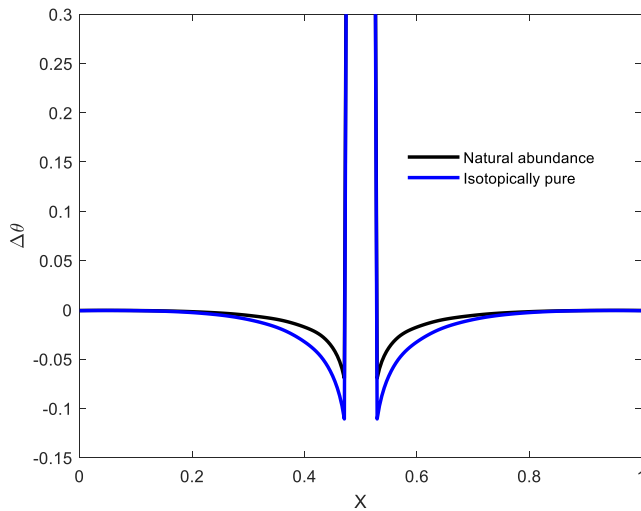


Fig. 14. Non-local temperature response between the upper edge and lower edge of the rectangular graphene ribbon with $L=15\mu\text{m}$, $T_0=100\text{K}$: the blue line represents the isotopically pure graphene (0% ^{13}C), whereas the black line represents the graphene with natural abundance (1.1% ^{13}C). Here $\Delta\theta$ is the difference of dimensionless temperature between the upper edge ($y=W$) and the lower edge ($y=0$).

Table 1
Spatial grid number for different cavity height-width ratios in the T-type graphene ribbon

H/L_1	N_x	N_y
1	240	160
2	240	240
3	240	320
4	240	400
5	240	480

bon length will severely deteriorate the hydrodynamic effect. The size effect shown in Fig. 10 and Fig. 11 at the average temperature 100K can be understood in a similar way. For the graphene ribbon length of around 100 μm , it is seen in Fig. 12(a) that only the phonons with $\omega < \sim 5\text{THz}$ well satisfy the hydrodynamic win-

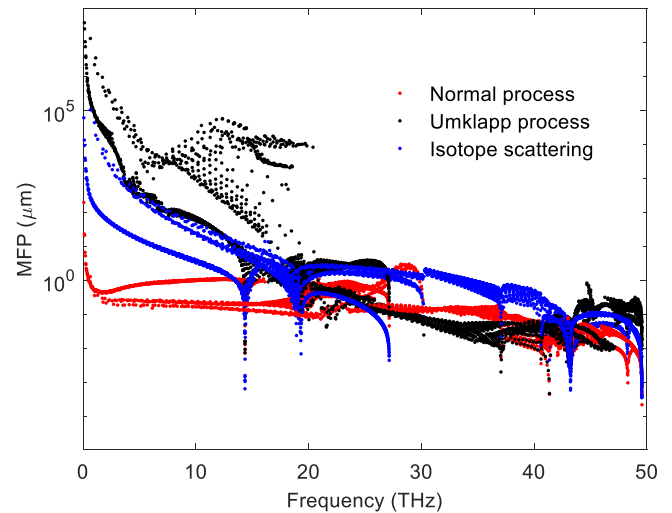


Fig. 15. Frequency-dependent mean free path (MFP) of normal, Umklapp and isotope scattering processes in graphene with natural abundance (1.1% ^{13}C) at 100K: the red points represent the normal process, the black points represent the Umklapp process, and the blue points represent the isotope scattering process.

down condition. As shown in Fig. 13(b), there are still appreciable phonons at $\omega > \sim 5\text{THz}$ which contribute to the average MFP and will destroy the hydrodynamic effect of the lower-frequency phonons. The present analysis indicates the strong destroying effect of resistive phonon scattering on hydrodynamic heat transport, which only happens when most of the dominant phonons lie in the window condition.

4.1.2. Isotope effect

The phonon vortex dynamics in the rectangular graphene ribbon with a length 15 μm and natural abundance (1.1% ^{13}C) at 100K is simulated to investigate the influence of isotope scattering. The size of phonon vortex is found to be reduced (not shown here to avoid repetition of similar figures) comparing to that in the isotopically pure case in Section 4.1.1. This is attributed to the resistive nature of isotope phonon scattering, which will destroy the phonon quasi-momentum and the hydrodynamic effect. Thus the non-local temperature response between the upper edge and lower

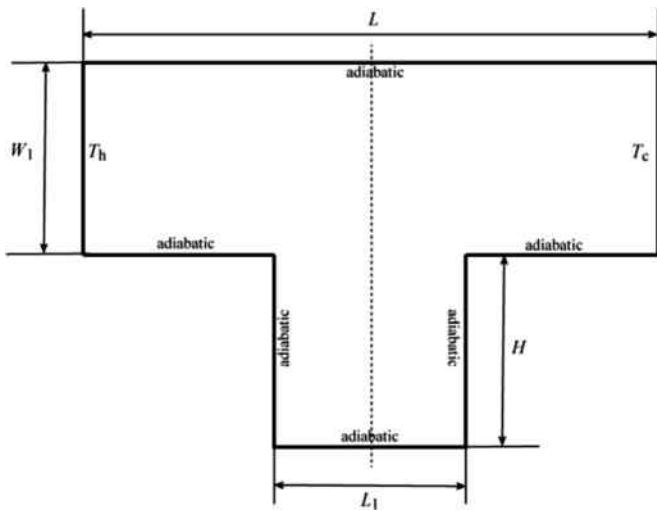


Fig. 16. Schematic of the physical model of phonon vortex in a T-type graphene ribbon

edge of the graphene ribbon with natural abundance will also be weakened as it is demonstrated in Fig. 14. A more quantitative understanding can be acquired through the MFP of different phonon scattering processes shown in Fig. 15. For the low- and moderate-frequency ($< \sim 14$ THz) phonons which dominate the contribution to heat transport at 100K, the MFP of isotope scattering is generally shorter than that of Umklapp scattering. In other words, the

isotope scattering is more resistive than the Umklapp scattering and determines the overall resistive scattering MFP, which makes the hydrodynamic window narrower.

4.2. Phonon vortex in T-type graphene ribbon

As the geometry of the graphene ribbon may be more complex than the rectangular one in actual heat dissipation application [12], we consider phonon heat transport in a T-type isotopically pure graphene ribbon with $L = 3W_1 = 3L_1 = 15\mu\text{m}$ shown in Fig. 16. The graphene ribbon consists of a horizontal rectangular part with fixed size and a cavity part with a variable height-width ratio H/L_1 . In the hydrodynamic regime, phonon transport in such a structure is similar to the lid-driven cavity flow [50], and phonon vortex is expected to exist in the cavity part. A small temperature difference of $T_h - T_c = 1\text{K}$ around an average system temperature T_0 is exerted on the horizontal rectangular part of the graphene ribbon. The influence of T_0 and H/L_1 on the phonon vortex configurations will be studied in this sub-section. After independence verification, a spectral grid of $NL = NT = NZ = 10$ for LA, TA and ZA phonons, and an angular grid of $N_\theta = 48$ are adopted in the DOM numerical solution. To ensure a uniform grid step, the spatial grid number is dependent on the cavity height-width ratio, as summarized in Table 1.

The phonon vortex dynamics in the T-type graphene ribbon with a fixed cavity height-width ratio of $H/L_1 = 1$ at three different average temperatures 100K, 150K and 300K are shown in Fig. 17. A transition from hydrodynamic heat transport at 100K to diffusive heat transport at 300K similar to that in Fig. 8 is ob-

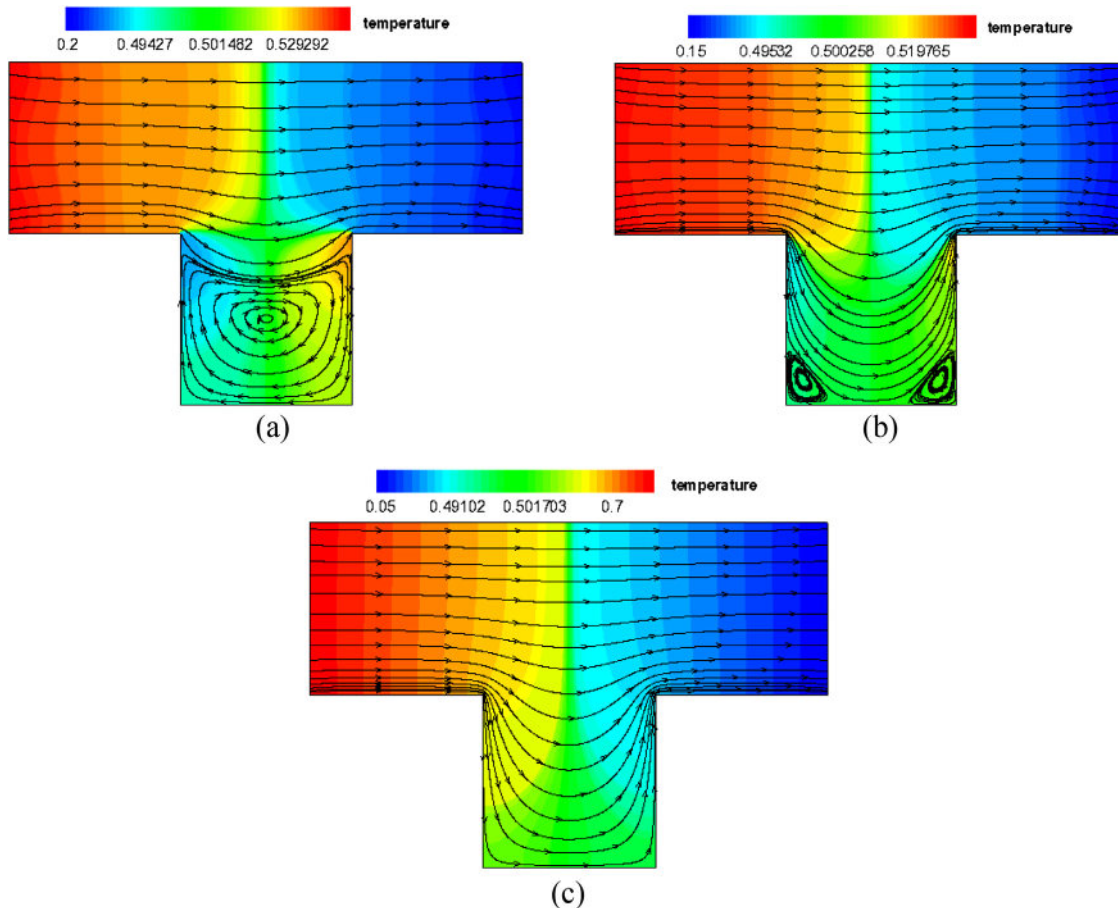


Fig. 17. Phonon cavity flow in a T-type graphene ribbon with $H/L_1 = 1$ at different average temperatures: (a) $T_0 = 100\text{K}$, (b) $T_0 = 150\text{K}$, (c) $T_0 = 300\text{K}$. The color contour denotes the distribution of the dimensionless temperature defined as: $\theta = (T - T_c) / (T_h - T_c)$, whereas the streamline denotes the heat flux vector.

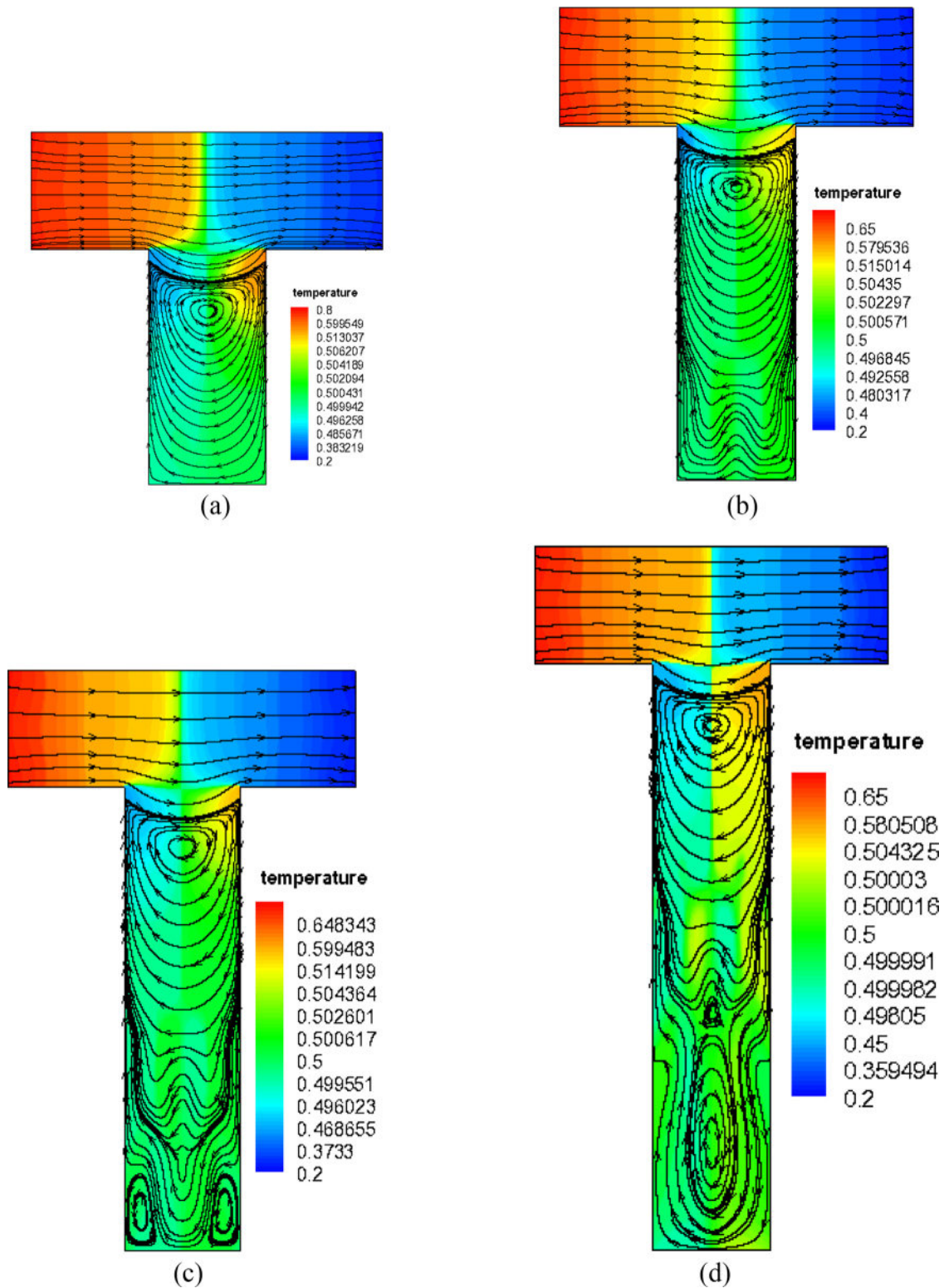


Fig. 18. Phonon cavity flow in a T-type graphene ribbon with different cavity height-width ratio at 100K: (a) $H/L_1=2$, (b) $H/L_1=3$, (c) $H/L_1=4$, (d) $H/L_1=5$. The color contour denote the distribution of dimensionless temperature defined as: $\theta=(T-T_c)/(T_h-T_c)$, whereas the streamline denotes the heat flux vector.

tained. At 100K, a large phonon vortex occupying the entire cavity part is generated by the ‘viscous force’ transferred from the phonons in the horizontal rectangular part. This vortex configuration resembles that in the lid-driven cavity fluid flow at low Reynolds number [55]. A negative non-local temperature response is also shown around the two upper corners of the cavity part.

As the average system temperature increases to 150K, both the phonon vortex and negative non-local response are reduced a lot due to the stronger Umklapp scattering. The phonon heat transport becomes diffusive at room temperature (300K) where the hydrodynamic effect is almost destroyed by the Umklapp phonon scattering.

It is known that the vortex configurations are very different for different aspect ratios in the cavity fluid flow [55]. The phonon vortex dynamics in the T-type graphene ribbon with four other cavity height-width ratios ($H/L_1=2, 3, 4, 5$) at a fixed average system temperature $T_0 = 100\text{K}$ are demonstrated in Fig. 18. Generally the phonon vortex pattern becomes more complicated with increasing cavity height-width ratio. There is still only one primary phonon vortex for $H/L_1=2$ in Fig. 18(a) as the same as that for $H/L_1=1$. As H/L_1 increases to 3, there is emerging instability of phonon flow near the cavity bottom in Fig. 18(b), which becomes the source of generation of a secondary vortex pair at a larger height-width ratio of $H/L_1=4$ in Fig. 18(c). At an even larger height-width ratio of $H/L_1 = 5$, both a small secondary vortex and a large ternary vortex appear, as shown in Fig. 18(d). The rotation direction of the secondary vortex and the ternary vortex is the reverse of and the same as that of the primary vortex respectively, which can be easily understood from the force interaction law (Newton's third law). The center position of the primary phonon vortex almost does not change with the cavity height-width ratio, since it is generated by the same 'viscous force' from phonons in the horizontal rectangular part.

Finally, we would like to emphasize that the unstrained graphene ribbon with an optimized lattice constant has been considered throughout the present work. The effect of strain on heat transport in graphene especially the convergence of thermal conductivity with size is quite complicated and remains still inconclusive [31,33,46] due to both the computational challenge and the lack of clear experimental evidence. Generally the strain will harden the ZA phonons (make the dispersion relation more linear) of 2D materials, as demonstrated in graphene [33,46] and in a diamond-like bi-layer graphene recently [56]. The hardening of ZA phonons will reduce both its density of states and the phase space channels for normal scattering processes, and thus weaken the phonon hydrodynamic effect. As the ZA phonons dominate the contribution to heat transport in graphene [31,32], it is anticipated that the strain will suppress the hydrodynamic phonon transport and the strength of phonon vortex. A direct study on the strain effect on the relative strength of normal and Umklapp scattering in graphene is pending in the future work.

5. Conclusions

In the present work, a multi-scale numerical framework is developed by combining the discrete-ordinate method for solving the phonon Boltzmann equation under Callaway's dual relaxation model with the phonon scattering rates from *ab initio* calculation. The new numerical framework is applied to study the phonon vortex dynamics in both a rectangular and a T-type graphene ribbon. The transition from hydrodynamic heat transport to classical diffusive heat transport is demonstrated in both cases. The dynamics of phonon vortex in the graphene ribbon is much influenced by the temperature, ribbon size and carbon isotope. The wide mean free path distribution of resistive phonon scattering processes is the crucial factor that destroys the vortex hydrodynamic effect. The phonon vortex configuration in the T-type graphene ribbon is found to depend on the height-width ratio, with multi-hierarchy primary, secondary and ternary vortices obtained. This work provides an efficient platform for the direct modeling of hydrodynamic phonon heat transport in finite-size graphitic materials. The understanding of phonon vortex dynamics in the graphene ribbon will also shed implication for the thermal management of semiconductor nano-electronics.

Declaration of Competing Interest

We declare that there is no conflict of interests for this work.

CRedit authorship contribution statement

Yangyu Guo: Conceptualization, Investigation, Writing - original draft, Funding acquisition. **Zhongwei Zhang:** Data curation. **Masahiro Nomura:** Project administration, Writing - review & editing. **Sebastian Volz:** Writing - review & editing. **Moran Wang:** Supervision, Project administration.

Acknowledgements

This work was supported by the Postdoctoral Fellowship of Japan Society for the Promotion of Science (P19353), CREST Japan Science and Technology Agency (JPMJCR1911 and JPMJCR19Q3), NSFC project (No. 51621062) and Tsinghua University Initiative Scientific Research Program. Y. Guo would like to appreciate helpful discussions with Z. Ding at MIT and X. Luo from HIT. This research used the computational resource of the Oakforest-PACS supercomputer system, The University of Tokyo.

References

- [1] S. Datta, Quantum transport: atom to transistor, Cambridge University Press, New York, 2005.
- [2] K. Hirose, N. Kobayashi, Quantum transport calculations for nanosystems, Pan Stanford Publishing, Singapore, 2014.
- [3] A.L. Moore, L. Shi, Emerging challenges and materials for thermal management of electronics, *Materials Today* 17 (2014) 163–174.
- [4] J. Cho, Z. Li, M. Asheghi, K.E. Goodson, Near-junction thermal management: Thermal conduction in gallium nitride composite substrates, *Annual Review of Heat Transfer* 18 (2015) 7–45.
- [5] D.G. Cahill, P.V. Braun, G. Chen, D.R. Clarke, S. Fan, K.E. Goodson, P. Keblinski, W.P. King, G.D. Mahan, A. Majumdar, H.J. Maris, S.R. Phillpot, E. Pop, L. Shi, Nanoscale thermal transport. II. 2003–2012, *Applied Physics Reviews* 1 (2014) 011305.
- [6] Y.Y. Guo, M.R. Wang, Phonon hydrodynamics and its applications in nanoscale heat transport, *Physics Reports* 595 (2015) 1–44.
- [7] S. Volz, J. Ordóñez-Miranda, A. Shchepetov, M. Prunnila, J. Ahopelto, T. Pezeril, G. Vaudel, V. Gusev, P. Ruello, E.M. Weig, M. Schubert, M. Hettich, M. Grossman, T. Dekorsy, F. Alzina, B. Graczykowski, E. Chavez-Angel, J. Sebastian Reparaz, M.R. Wagner, C.M. Sotomayor-Torres, S. Xiong, S. Neogi, D. Donadio, Nanophononics: state of the art and perspectives, *European Physical Journal B* 89 (2016) 15.
- [8] M. Nomura, J. Shiomi, T. Shiga, R. Anufriev, Thermal phonon engineering by tailored nanostructures, *Japanese Journal of Applied Physics* 57 (2018) 080101.
- [9] Z. Zhang, Y. Ouyang, Y. Cheng, J. Chen, N. Li, G. Zhang, Size-dependent phononic thermal transport in low-dimensional nanomaterials, *Physics Reports* 860 (2020) 1–26.
- [10] E. Pop, V. Varshney, A.K. Roy, Thermal properties of graphene: Fundamentals and applications, *MRS Bulletin* 37 (2012) 1273–1281.
- [11] D.L. Nika, A.A. Balandin, Phonons and thermal transport in graphene and graphene-based materials, *Reports on Progress in Physics* 80 (2017) 036502.
- [12] Z. Yan, G. Liu, J. Khan, A. Balandin, Graphene quilts for thermal management of high-power GaN transistors, *Nature Communications* 3 (2012) 827.
- [13] H. Han, Y. Zhang, N. Wang, M.K. Samani, Y. Ni, Z.Y. Mijbil, M. Edwards, S. Xiong, K. Sääskilähti, M. Murugesan, Y. Fu, L. Ye, H. Sedeghi, S. Bailey, Y.A. Kosevich, C.J. Lambert, J. Liu, S. Volz, Functionalization mediates heat transport in graphene nanoflakes, *Nature Communications* 7 (2016) 11281.
- [14] A. Cepellotti, G. Fugallo, L. Paulatto, M. Lazzeri, F. Mauri, N. Marzari, Phonon hydrodynamics in two-dimensional materials, *Nature Communications* 6 (2015) 6400.
- [15] S. Lee, D. Broido, K. Esfarjani, G. Chen, Hydrodynamic phonon transport in suspended graphene, *Nature Communications* 6 (2015) 6290.
- [16] S. Huberman, R.A. Duncan, K. Chen, B. Song, V. Chiloian, Z. Ding, A.A. Maznev, G. Chen, K.A. Nelson, Observation of second sound in graphite at temperatures above 100 K, *Science* 364 (2019) 375–379.
- [17] S. Lee, X. LiB. Liao (Ed.), Hydrodynamic phonon transport: past, present and prospects, *Nanoscale Energy Transport: Emerging phenomena, methods and applications* (2020) 1–26.
- [18] Y. Guo, M. Wang, Heat transport in two-dimensional materials by directly solving the phonon Boltzmann equation under Callaway's dual relaxation model, *Physical Review B* 96 (2017) 134312.
- [19] X. Li, S. Lee, Role of hydrodynamic viscosity on phonon transport in suspended graphene, *Physical Review B* 97 (2018) 094309.
- [20] X. Li, S. Lee, Crossover of ballistic, hydrodynamic, and diffusive phonon transport in suspended graphene, *Physical Review B* 99 (2019) 085202.
- [21] S. Lee, X. Li, R. Guo, Thermal resistance by transition between collective and non-collective phonon flows in graphitic materials, *Nanoscale and Microscale Thermophysical Engineering* 23 (2019) 247–258.
- [22] R. Yang, S. Yue, B. Liao, Hydrodynamic phonon transport perpendicular to diffuse-gray boundaries, *Nanoscale and Microscale Thermophysical Engineering* 23 (2019) 25–35.

- [23] A.K. Majee, Z. Aksamija, Dynamical thermal conductivity of suspended graphene ribbons in the hydrodynamic regime, *Physical Review B* 98 (2018) 024303.
- [24] X.-P. Luo, Y.-Y. Guo, M.-R. Wang, H.-L. Yi, Direct simulation of second sound in graphene by solving the phonon Boltzmann equation via a multiscale scheme, *Physical Review B* 100 (2019) 155401.
- [25] B.-D. Nie, B.-Y. Cao, Thermal Wave in Phonon Hydrodynamic Regime by Phonon Monte Carlo Simulations, *Nanoscale and Microscale Thermophysical Engineering* 24 (2020) 94–122.
- [26] M. Simoncelli, N. Marzari, A. Cepellotti, Generalization of Fourier's law into viscous heat equations, *Physical Review X* 10 (2020) 011019.
- [27] L. Levitov, G. Falkovich, Electron viscosity, current vortices and negative non-local resistance in graphene, *Nature Physics* 12 (2016) 672–676.
- [28] D. Bandurin, I. Torre, R.K. Kumar, M.B. Shalom, A. Tomadin, A. Principi, G. Auton, E. Khestanova, K. Novoselov, I. Grigorieva, Negative local resistance caused by viscous electron backflow in graphene, *Science* 351 (2016) 1055–1058.
- [29] A. Lucas, K.C. Fong, Hydrodynamics of electrons in graphene, *Journal of Physics: Condensed Matter* 30 (2018) 053001.
- [30] M.-Y. Shang, C. Zhang, Z. Guo, J.-T. Lü, Heat vortex in hydrodynamic phonon transport of two-dimensional materials, *Scientific Reports* 10 (2020) 8272.
- [31] L. Lindsay, W. Li, J. Carrete, N. Mingo, D. Broido, T. Reinecke, Phonon thermal transport in strained and unstrained graphene from first principles, *Physical Review B* 89 (2014) 155426.
- [32] L. Lindsay, D. Broido, N. Mingo, Flexural phonons and thermal transport in graphene, *Physical Review B* 82 (2010) 115427.
- [33] G. Fugallo, A. Cepellotti, L. Paulatto, M. Lazzeri, N. Marzari, F. Mauri, Thermal conductivity of graphene and graphite: collective excitations and mean free paths, *Nano Letters* 14 (2014) 6109–6114.
- [34] C.D. Landon, N.G. Hadjiconstantinou, Deviation simulation of phonon transport in graphene ribbons with ab initio scattering, *Journal of Applied Physics* 116 (2014) 163502.
- [35] J. Callaway, Model for lattice thermal conductivity at low temperatures, *Physical Review* 113 (1959) 1046–1051.
- [36] J. Ma, W. Li, X. Luo, Examining the Callaway model for lattice thermal conductivity, *Physical Review B* 90 (2014) 035203.
- [37] A.K. Majee, Z. Aksamija, Length divergence of the lattice thermal conductivity in suspended graphene nanoribbons, *Physical Review B* 93 (2016) 235423.
- [38] S. Lee, L. Lindsay, Hydrodynamic phonon drift and second sound in a (20, 20) single-wall carbon nanotube, *Physical Review B* 95 (2017) 184304.
- [39] Z. Ding, J. Zhou, B. Song, V. Chiloyan, M. Li, T.-H. Liu, G. Chen, Phonon hydrodynamic heat conduction and Knudsen minimum in graphite, *Nano Letters* 18 (2018) 638–649.
- [40] Q. Hao, G. Chen, M.-S. Jeng, Frequency-dependent Monte Carlo simulations of phonon transport in two-dimensional porous silicon with aligned pores, *Journal of Applied Physics* 106 (2009) 114321.
- [41] A. Majumdar, Microscale Heat Conduction in dielectric Thin Films, *Journal of Heat Transfer* 115 (1993) 7–16.
- [42] S. Volz, D. Lemonnier, J.-B. Saulnier, Clamped nanowire thermal conductivity based on phonon transport equation, *Microscale Thermophysical Engineering* 5 (2001) 191–207.
- [43] R.G. Yang, G. Chen, M. Laroche, Y. Taur, Simulation of nanoscale multidimensional transient heat conduction problems using ballistic-diffusive equations and phonon Boltzmann equation, *Journal of Heat Transfer* 127 (2005) 298–306.
- [44] P. Giannozzi, S. Baroni, N. Bonini, M. Calandra, R. Car, C. Cavazzoni, D. Ceresoli, G.L. Chiarotti, M. Cococcioni, I. Dabo, QUANTUM ESPRESSO: a modular and open-source software project for quantum simulations of materials, *Journal of Physics: Condensed Matter* 21 (2009) 395502.
- [45] A. Taheri, C. Da Silva, C.H. Amon, First-principles phonon thermal transport in graphene: Effects of exchange-correlation and type of pseudopotential, *Journal of Applied Physics* 123 (2018) 215105.
- [46] Y. Kuang, L. Lindsay, S. Shi, X. Wang, B. Huang, Thermal conductivity of graphene mediated by strain and size, *International Journal of Heat Mass Transfer* 101 (2016) 772–778.
- [47] A. Togo, I. Tanaka, First principles phonon calculations in materials science, *Scripta Materialia* 108 (2015) 1–5.
- [48] W. Li, J. Carrete, N.A. Katcho, N. Mingo, ShengBTE: A solver of the Boltzmann transport equation for phonons, *Computer Physics Communications* 185 (2014) 1747–1758.
- [49] M. Park, S.-C. Lee, Y.-S. Kim, Length-dependent lattice thermal conductivity of graphene and its macroscopic limit, *Journal of Applied Physics* 114 (2013) 053506.
- [50] J. Koseff, R. Street, The lid-driven cavity flow: a synthesis of qualitative and quantitative observations, *Journal of Fluids Engineering* 106 (1984) 390–398.
- [51] S.R. De Groot, P. Mazur, *Non-equilibrium thermodynamics*, Dover Publications, New York, 1962.
- [52] R.A. Guyer, J.A. Krumhansl, Thermal conductivity, second sound, and phonon hydrodynamic phenomena in nonmetallic crystals, *Physical Review* 148 (1966) 778–788.
- [53] D. Jou, J. Casas-Vázquez, G. Lebon, *Extended irreversible thermodynamics*, Springer, Heidelberg, 2010.
- [54] Y. Guo, M. Wang, Thermodynamic analysis of gas flow and heat transfer in microchannels, *International Journal of Heat and Mass Transfer* 103 (2016) 773–782.
- [55] L.-S. Lin, Y.-C. Chen, C.-A. Lin, Multi relaxation time lattice Boltzmann simulations of deep lid driven cavity flows at different aspect ratios, *Computers & Fluids* 45 (2011) 233–240.
- [56] Y. Hu, D. Li, Y. Yin, S. Li, G. Ding, H. Zhou, G. Zhang, The important role of strain on phonon hydrodynamics in diamond-like bi-layer graphene, *Nanotechnology* 31 (2020) 335711.